

Informational entropic Regge trajectories of meson families in AdS/QCD

A. E. Bernardini¹ and R. da Rocha^{2,*}

¹*Departamento de Física, Universidade Federal de São Carlos,
PO Box 676, 13565-905, São Carlos, SP, Brazil*[†]

²*Federal University of ABC, Center of Mathematics,
Computing and Cognition, Santo André, Brazil*^{*}

Bulk mesons propagating in chiral and gluon condensates, in a gravity background, are scrutinized in holographic soft wall AdS/QCD models, involving deformed dilatonic backgrounds. The configurational entropy of the a_1 axial vector, the ρ vector, and the f_0 scalar meson families is then computed. Two types of informational entropic Regge trajectories are then obtained, where the logarithm of the mesons configurational entropy is expressed in terms of both the experimental meson mass spectra and their excitation number as well. Therefore the mass spectra of the next generation of elements in each meson family, besides being predicted as eigenvalues of Schrödinger-like equations, are estimated with better accuracy and discussed.

PACS numbers: 89.70.Cf, 11.25.Tq, 14.40.Be

I. INTRODUCTION

The Shannon's information entropy paradigm resides in encoding information in stochastic processes [1]. The configurational entropy (CE) is a quantity that implements the information entropy as a measure that logarithmically evaluates the number of bits needed to designate the organization of a system. In particular, the CE comprehends the information compression into the configuration of wave modes in a physical system [2, 3]. Among the so called configurational information-measures [4], the CE encompasses the informational quantification of the spatial complexity of a localized system [5, 6]. The wave modes and particle excitations, that are correlated to critical points of the CE, have been shown to be more dominant or abundant among all other modes and, hence, more detectable or observable in Nature [7–9]. The CE plays a relevant role in the study of phase transitions, that are also driven by critical points of the CE, underlying diverse physical systems [5, 6, 10, 11]. A meticulous overview on the information entropy formalism can be seen in Ref. [12].

Quantum chromodynamics (QCD) governs the strong interactions among gluons and quarks. The AdS/QCD holographic setup presents an AdS₅ bulk¹, wherein gravity, that is weakly coupled, emulates the dual setup to the 4d (conformal) field theory (CFT), that is strongly coupled on the AdS₅ boundary. In the duality dictionary, physical fields in the AdS₅ bulk are dual objects to 4d operators of QCD [13]. It is worth to mention that the bulk fifth dimension is nothing more than the energy scale of the theory. Confinement can be then implemented either by a Heaviside cut-off in the bulk – the hard wall [14, 15] – or by a dilatonic field, that ac-

complishes a smooth cut-off along the AdS₅ bulk – the soft wall model [16, 17]. From a phenomenological point of view, the quark-gluon plasma (QGP), the mesonic mass spectra and their Regge trajectories [18] and other quantities were derived, using the holographic soft wall AdS/QCD, being precisely corroborated by experimental data [19]. Soft wall AdS/QCD models implement the (chiral) symmetry breaking [20, 21] and confinement as well [17, 22, 23]. In particular, mesonic phenomenology can be thus allocated into the soft wall AdS/QCD. As shall be used throughout this paper, although QCD is driven by a SU(3) gauge symmetry, one can supersede it by a SU(N_c) group. Hence, the so called 't Hooft large- N_c limit [24] plays an important role on the soft wall.

In the above discussed context, the CE has been recently promoted to a relevant setup in the context of holographic AdS/QCD models. Besides probing important informational aspects of the AdS/QCD, the CE also supports some foundations to better understand mesonic states in QCD phenomenology. Some of the existing experimental data regarding meson families and glueball states were corroborated by the CE, that points into the direction of the most abundant and dominant physical states in QCD, in an intense research program. In fact, holographic AdS/QCD models were first scrutinized, in the CE framework, in Refs. [7–9]. Mesonic excitations with lower s -wave resonances were proved, in Ref. [7], to present dominance over their higher s -wave counterparts. Thereafter, the CE paradigm was employed to scrutinize scalar glueball states in Ref. [8], corroborating to lattice and experimental data [19]. In addition, the CE of dynamical AdS/QCD with tachyonic potentials improved our understanding about mesons phenomenology in Ref. [25]. Moreover, the CE that underlies bottomonium and charmonium states at zero temperature supports the experimental rareness of quarkonia states with higher masses, as discussed in Ref. [9]. The finite temperature case was then implemented in Ref. [26], with unexpected and relevant quarkonia new features. Finally, QGPs with topological defects were also explored in the

*Electronic address: roldao.rocha@ufabc.edu.br

[†]Electronic address: alexeb@ufscar.br

¹ Anti-de Sitter.

CE setup [27]. The CE also improved the understanding of the AdS/QCD light-front wave function, where the color-glass condensate regime was used to study mesons in Refs. [28–31]. With the CE tools, heavy ion collisions were also studied [32]. Furthermore, aspects of the CE unraveled prominent features of the gravity side of AdS/QCD and related phenomena. The Hawking–Page phase transition was studied in Ref. [11] in the context of the CE. Posterior to the influential works [33, 34], graviton condensates were explored with by the CE, in AdS/CFT membrane paradigm [35]. The CE apparatus was further employed in field theory, in various contexts [36–39].

Here one big step further is aimed, besides corroborating to experimental data of a_1 axial vector, the ρ vector, and the f_0 scalar mesons families. Using both the quadratic and deformed dilatonic backgrounds, informational entropic Regge trajectories shall be derived, relating the logarithm of the CE to the n excitation number of mesonic states, for each one of the meson families. The mesons mass spectra are well known to be predicted in the soft wall AdS/QCD, with good accuracy. In fact, for both the dilatonic backgrounds, the equations of motion (EOMs) of a graviton-dilaton-gluon action are equivalent to Schrödinger-like equations, whose eigenvalues consist of the meson squared mass spectra. Their eigenfunctions represent the mesonic states and excitations, for the a_1 axial vector, the ρ vector, and the f_0 scalar mesons families. The CE for these meson families shall be also computed with respect to the meson families mass spectra, revealing a second type of informational entropic Regge trajectories. Hence, one can extrapolate the meson mass spectra from these informational entropic Regge trajectories, also predicting the mass of the next generation of elements in each meson family, corresponding to higher n excitation numbers, with good accuracy. The masses of the first mesonic excitations of the next generation, in each meson family, shall be then estimated and discussed.

This article is devised as follows: Sect. II is devoted to briefly review the soft wall AdS/QCD framework, mainly emphasizing the standard quadratic dilaton model. The mass spectra of ρ vector, a_1 axial vector, and f_0 scalar mesonic states shall be revised. Sect. III is dedicated to introduce the chiral and gluon condensates, with a two flavor system in the graviton-dilaton-gluon setup, for both the quadratic and deformed dilatonic fields. In Sect. IV, the CE is computed for the a_1 axial vector, the ρ vector, and the f_0 scalar mesons families, as a function of the n excitation number. Hence, informational entropic Regge trajectories are read off these calculations, showing a relation between the logarithm of the CE, for all regarded mesons families, and their n excitation modes. Besides, the meson mass spectra for higher excitation numbers can be also extracted from a second kind of informational entropic Regge trajectories, that relate the logarithm of the CE and the meson mass spectra, for each meson family. Hence, the mass spectra of higher n excited mesonic states, in each meson family, are esti-

mated with good accuracy. In Sect. V, our concluding remarks, outlook, and perspectives are drawn

II. SOFT WALL ADS/QCD

The AdS_5 vacuum bulk has a 4d boundary, that supports a gauge theory, that is conformally invariant, emulating the standard QCD when $N_c \gg 1$. The boundary conformal symmetry can be broken, making QCD to describe the confinement. In this regime, gravity in the bulk is dual to the QCD at the boundary. A straightforward way to break the boundary symmetry is, for example, to endow the AdS bulk with a dilatonic field. Since QCD approximately recovers conformal symmetries, in a high energy regime, then the pure AdS bulk must prevail in the ultraviolet (UV) regime.

Mesons families can be emulated in the holographic soft wall AdS/QCD [17, 40] and in its extended versions [20, 23, 41, 42], including the dynamical models [25, 43–46] and scalars and vector mesonic states [47]. The Regge trajectories for excited light-flavor mesons were originally derived in Ref. [17], on a soft wall model endowed with a quadratic dilaton, $\Phi(z) = \mu^2 z^2$, where μ introduces an energy scale in QCD [48]. The AdS_5 background bulk metric is expressed, in conformal coordinates, as

$$ds^2 = g_{mn} dx^m dx^n = e^{2A(z)} (\eta_{\mu\nu} dx^\mu dx^\nu + dz^2), \quad (1)$$

for the warp factor $A(z) = -\log(z/\ell)$, where the $\eta_{\mu\nu}$ denote the 4d space-time metric components and ℓ is related to the bulk curvature radius. Other warp factors, extending the soft wall AdS/QCD, were used in Refs. [44, 45, 49].

Hereon m, n, q denote bulk indexes, running from 0 to 4, where $x^m = (x^\mu, x^4)$, for x^μ denoting 4d space-time coordinates and x^4 denoting the bulk coordinate. Light-flavor mesonic excitations are represented by bulk $\mathfrak{X}(z)$ fields, that are dual objects to the quark-antiquark operator, with associated mass $m_{\mathfrak{X}}$, and governed by the action [17]

$$S = - \int e^{-\Phi(z)} \sqrt{-g} \text{Tr } \mathfrak{L} d^5x, \quad (2)$$

where

$$\mathfrak{L} = D_m \mathfrak{X} D^m \mathfrak{X} + m_{\mathfrak{X}}^2 \mathfrak{X}_m \mathfrak{X}^m + \frac{N_c}{48\pi^2} (F_R^2 + F_L^2), \quad (3)$$

where the A_L^m and A_R^m gauge fields drive the $\text{SU}(2)_L \times \text{SU}(2)_R$ chiral flavor symmetry of QCD. Each $\text{SU}(2)$, with $\{f_b/2\}$ ($b = 1, 2, 3$) generators, correspond to one quark flavor. The left and right gauge field strengths respectively read

$$F_{L,R}^{mn} = \partial^{[m} A_{L,R}^{n]} - i[A_{L,R}^m, A_{L,R}^n], \quad (4)$$

where $A_{L,R}^m = A_{L,R}^{ma} f_a$. The covariant derivative is explicitly given by $D^m \mathfrak{X} = \partial^m \mathfrak{X} - i A_L^m \mathfrak{X} + i \mathfrak{X} A_R^m$. The $\mathfrak{X}(z)$

field incorporates the S (scalar) and P (pseudo-scalar) fields, as [50]

$$\mathfrak{X}(z) = (S + \xi(z)) \exp(iP^b t^b), \quad (5)$$

where $\xi(z)$ is a vacuum expectation value that breaks chiral symmetry [50]. To describe the vector and axial vector meson, the left, A_L , and right, A_R , gauge fields can be split into the vector (V) and axial vector (\mathring{A}) fields, as [50]

$$V^m = (A_R^m + A_L^m)/2 \quad (6a)$$

$$\mathring{A}^m = (A_R^m - A_L^m)/2, \quad (6b)$$

yielding the respective gauge field strengths,

$$F_V^{mn} = \partial^{[m} V^{n]}, \quad (7)$$

$$F_{\mathring{A}}^{mn} = \partial^{[m} \mathring{A}^{n]} - i[\mathring{A}^m, \mathring{A}^n]. \quad (8)$$

With respect to the vector V and axial vector \mathring{A} fields, the soft wall Lagrangian (3) reads

$$\mathcal{L} = D_m \mathfrak{X} D^m \mathfrak{X} + m_{\mathfrak{X}}^2 \mathfrak{X}_m \mathfrak{X}^m + \frac{N_c}{24\pi^2} (F_{\mathring{A}}^2 + F_V^2), \quad (9)$$

for $D_m = \partial_m \mathfrak{X} + i(XV_m - V_m X - A_m X - X A_m)$. The EOM for the $\xi(z)$ field then reads

$$\xi''(z) + (3A'(z) - \Phi'(z))\xi'(z) - m_{\mathfrak{X}}^2(z)e^{2A(z)}\xi(z) = 0. \quad (10)$$

In the standard soft wall model, $\Phi(z) = \mu^2 z^2$ [17], and Eq. (10) has solutions

$$\xi(z) = c_1 z^3 \exp(z^2/2) I(z) + c_2 G_{12}^{20} \left(-z^2 \Big| \begin{matrix} 1 \\ 1/2, 3/2 \end{matrix} \right), \quad (11)$$

with $I(z) = I_0\left(\frac{z^2}{2}\right) + I_1\left(\frac{z^2}{2}\right)$, where $I_n(z)$ denotes the first kind modified Bessel function, and the second term is the Meijer function of $\{1, 2; 2, 0\}$ order.

Let one denotes by v_n the functions that describe the ρ vector mesons, and by a_n those ones that represent the a_1 axial vector mesons, whereas the s_n denote the functions that comprise the f_0 scalar mesons. For the vector (ρ), axial vector (a_1), and scalar (f_0) meson families, for $n = 1, 2, \dots$, the meson spectra in the standard soft wall AdS/QCD model are ruled by the following EOMs [17],

$$\left(-\frac{d^2}{dz^2} + V_s(z) \right) s_n(z) = m_n^2 s_n(z), \quad (12)$$

$$\left(-\frac{d^2}{dz^2} + V_{\rho}(z) \right) v_n(z) = m_n^2 v_n(z), \quad (13)$$

$$\left(-\frac{d^2}{dz^2} + V_a(z) \right) a_n(z) = m_n^2 a_n(z), \quad (14)$$

where the Schrödinger-like potentials are respectively given by

$$V_s(z) = \frac{(\Phi'(z) - 3A'(z))^2 - 1}{4} - m_{\mathfrak{X}}^2 e^{2A(z)}. \quad (15)$$

$$V_{\rho}(z) = \frac{(\Phi'(z) - A'(z))^2 - 1}{4}, \quad (16)$$

$$V_a(z) = \frac{(\Phi'(z) - A'(z))^2 - 1}{4} + \frac{48\pi^2}{N_c} e^{2A(z)} \xi^2(z), \quad (17)$$

The potentials (15) – (17) respectively determine the mass spectra of the a_1 , ρ , and f_0 mesons families, as (squared) eigenvalues in Eqs. (12) – (14). The experimental data for the a_1 axial vector, the ρ vector, and the f_0 scalar mesons are shown in Fig. 1.

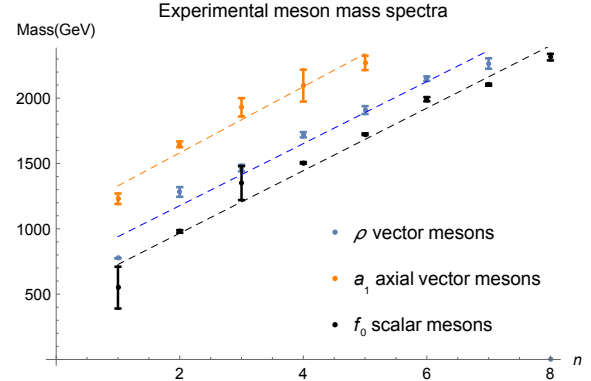


FIG. 1: Experimental mesonic states mass spectra with error bars [19], as a function of the n excitation number. The black points represent the $f_0(500)$, $f_0(980)$, $f_0(1370)$, $f_0(1500)$, $f_0(1710)$, $f_0(2020)$, $f_0(2200)$ and $f_0(2330)$ scalar mesons, whereas the blue points depict the $\rho(770)$, $\rho'(1450)$, $\rho(1450)$, $\rho(1570)$, $\rho(1700)$, $\rho(1900)$, $\rho(2150)$ and $\rho(2270)$ vector meson states. The orange points represent $a_1(1260)$, $a_1(1420)$, $a_1(1640)$, $a_1(1930)$, $a_1(2095)$ and $a_1(2270)$ axial vector mesons.

III. TWO FLAVOR SOFT WALL ADS/QCD IN GRAVITON-DILATON-GLUON BULK

A two flavor soft wall AdS/QCD can be then considered, where a dilatonic background field is assumed in a chiral and gluon condensate background, with gravity. For the pure gluon system, the scalar glueballs CE was already studied in Ref. [8]. Besides, Ref. [50] used two types of dilaton background fields, yielding the glueball spectra in full compliance to lattice data, namely

$$\Phi_1(z) = \mu_G^2 z^2, \quad (18)$$

$$\Phi_2(z) = \mu_G^2 z^2 \tanh\left(\frac{\mu_{G^2}^4 z^2}{\mu_G^2}\right). \quad (19)$$

The dual dimension-2 [dimension-4] gluon condensate has μ_G [μ_{G^2}] energy scale. The $\Phi_1(z)$ dilatonic field in Eq. (18) yields the meson spectra and also implements the quarks confinement [17]. It is the dual object to the gluon condensate with dimension-2, meaning the Bose–Einstein condensate consisting of strongly coupled paired gluons [16, 20, 42]. The $\Phi_2(z)$ dilatonic field in Eq. (19), at the UV regime behaves as $\lim_{z \rightarrow 0} \Phi_2(z) = \mu_{G^2}^4 z^4$, being dual to a gluon condensate that has dimension-4 [51]. At the IR regime, $\lim_{z \rightarrow \infty} \Phi_2(z) = \mu_G^2 z^2$.

A graviton-dilaton-gluon bulk action can be expressed as a sum of an Einstein–Hilbert action for pure gravity in the bulk, an action for gluons written with respect to the Φ dilaton field, and an action for two flavor bulk

mesons on a dilatonic background. This last part of the action implements the dynamics of the $\xi(z)$ scalar field in Eq. (5). The effective graviton-dilaton-gluon bulk action reads [50],

$$S = \kappa_5^2 \int \sqrt{-g} e^{-2\Phi} \left\{ [R/4 + g_{mn} \partial^m \Phi \partial^n \Phi - V_g(\Phi)] - 4\lambda e^{-\Phi} (g_{mn} \partial^m \xi \partial^n \xi + V(\Phi, \xi)) \right\} d^5x, \quad (20)$$

where λ denotes a general coupling, and V_g denotes the gluon system potential. The action (20) yields the following EOM:

$$-3A'' + 3A'^2 + 2\Phi'' - 4A'\Phi' - 2\lambda e^\Phi \xi'^2 = 0, \quad (21a)$$

$$8\Phi'' + 24A'\Phi' - 16\Phi'^2 - 6\lambda \xi'^2 e^\Phi$$

$$-3 \frac{\partial}{\partial \Phi} \left(\lambda e^{\tau\Phi/3} V(\Phi, \xi) + V_g(\Phi) \right) e^{-4\Phi/3 + 2A} = 0, \quad (21b)$$

$$-\xi'' + (\Phi' - 3A')\xi' + e^{2A} \frac{\partial^2 V(\Phi, \xi)}{\partial \xi \partial \Phi} = 0. \quad (21c)$$

In what follows N_f stands for the number of flavors. In the UV regime, Refs. [50, 52] show that $\lim_{z \rightarrow 0} \xi(z) = \frac{m_q \tau z}{2} + \frac{\sigma}{2\tau} z^3$, where m_q is the quark mass, σ denotes the string tension gluing the quark-antiquark condensate, and $\tau^2 = \frac{N_c^2}{4\pi^2 N_f}$, with $N_c = 3$ and $N_f = 2$. Ref. [50] scrutinized the heavy quark potential under the graviton-dilaton-gluon background (20), showing that the potential in (20) and (21c) reads $V(\Phi, \xi) \approx \xi^2 \Phi^2$, $\lim_{z \rightarrow \infty} A'(z) = 0$ and $\lim_{z \rightarrow \infty} A(z) = a$, for a a constant. For both the $\Phi_1(z)$ and $\Phi_2(z)$, respectively in Eqs. (18) and (19), the parameters $\mu_G = 0.43 = \mu_{G^2}$ were adopted in Ref. [50], in order to fit the meson spectra data with good accuracy to experimental data. Besides, $\sigma \approx 5.841 \times 10^6$ MeV and $m_q = 5.81$ MeV, for the $\Phi_1(z)$ quadratic dilaton, whereas $\sigma \approx 4.484 \times 10^6$ MeV and $m_q = 8.38$ MeV, for the $\Phi_2(z)$ deformed dilaton.

Numerical analysis of Eqs. (21a) – (21c) in Ref. [50] yield the solutions for $\xi(z)$, for both the dilatonic backgrounds, in Figs. 2 and 3, in full compliance with the UV and the IR regimes for the dilaton fields in Eqs. (18) and (19).

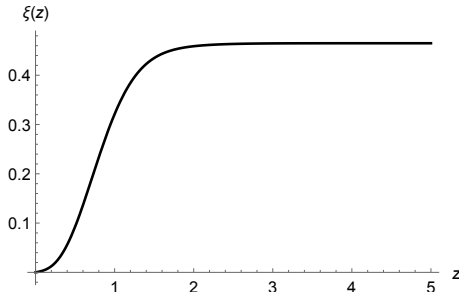


FIG. 2: $\xi(z)$ field, in the (18) quadratic dilatonic background.

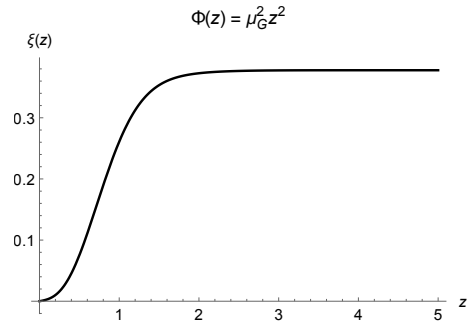


FIG. 3: $\xi(z)$ field, in the (19) deformed dilatonic background.

IV. INFORMATIONAL ENTROPIC REGGE TRAJECTORIES AND MESON MASS SPECTRA

The meson spectra was computed for the $\Phi_1(z)$ and $\Phi_2(z)$ dilaton backgrounds in Ref. [50]. Replacing Eqs. (18) – (19), and the scalar field $\xi(z)$ in Eqs. (21a) – (21c), one can derive the $A(z)$ warp factor. To obtain the S scalar mesons mass spectra, the following action was employed in Ref. [50]

$$S_s = \kappa \int e^{-\Phi} \sqrt{-g} (\partial_m S \partial^m S + 2S^2 \Phi^2) d^5x, \quad (22)$$

where $\partial_m S \partial^m S = \partial_z S \partial^z S + \partial_\mu S \partial^\mu S$, and $\kappa = -2 \frac{N_f}{N_c \ell^3}$. The EOM for the S scalar is given by Eq. (12), however with the Schrödinger potential

$$V_s(z) = \frac{1}{4}(\Phi' - 3A')^2 + \frac{3}{2}(3A'' - \Phi'') - \left(2A' - \frac{\Phi'}{2} + \frac{\Phi'}{2(1+\Phi)} \right) (3A' - \Phi') + \left(A' - \frac{3}{2}\Phi' - \frac{\Phi'}{2(1+\Phi)} \right) \log(2\xi')' + \frac{\xi'''}{\xi'}, \quad (23)$$

instead. The mass spectra for the f_0 scalar meson family is then forthwith obtained, being listed in the second and third rows of Table I, respectively for the quadratic (Eq. (18)) and the deformed (Eq. (19)) dilaton fields. It is accomplished by solving Eq. (12) with the potential in Eq. (23), using boundary condition $\lim_{z \rightarrow \infty} s_n'(z) = 0$ and $s_n(0) = 0$, with parameters $m_q \approx 9$ MeV and $\mu \approx 429$ MeV. The first column replicates the experimental masses in the PDG 2018 [19], respectively for the $f_0(500)$, $f_0(980)$, $f_0(1370)$, $f_0(1500)$, $f_0(1710)$, $f_0(2020)$, $f_0(2200)$ and $f_0(2330)$ mesons.

For deriving the mass spectra for the ρ meson family, for $\kappa = \frac{N_f}{2g_5^2 N_c \ell^3}$, the action

$$S_V = -\kappa \int e^{5A - \Phi} g_{\mu\nu} \partial_m V_\mu^\intercal \partial^m V^\nu d^5x, \quad (24)$$

is employed, where V_μ^\intercal denotes the transverse components in Eq. (15). The normalizable solutions, v_n , of the associated EOMs (13) – (16) are obtained as Kaluza–Klein modes for discrete values of the 4d momentum

f_0 scalar mesons mass spectra			
n	Exper. (MeV)	mass $_{\Phi_1(z)}$ (MeV)	mass $_{\Phi_2(z)}$ (MeV)
1	563 $^{+58}_{-69}$	420.9	186.9
2	990 \pm 20	1042.6	1077.8
3	1400 \pm 40	1369.5	1434.0
4	1504 \pm 6	1625.0	1684.5
5	1723 $^{+6}_{-5}$	1842.4	1889.7
6	1992 \pm 16	2035.7	2067.4
7	2189 \pm 13	2211.9	2233.8
8	2337 \pm 14	2374.8	2391.8

TABLE I: The experimental and predicted mass spectra for f_0 scalar mesons, in both the quadratic (18) (second column) and the deformed (19) (third column) dilaton profiles. Respectively along the rows, for the $f_0(500)$, $f_0(980)$, $f_0(1370)$, $f_0(1500)$, $f_0(1710)$, $f_0(2020)$, $f_0(2200)$ and $f_0(2330)$ mesons.

$q^2 = m_n^2$. The boundary fields v_μ (cf. Eq. (13)) play the role of external sources, coupled to the QCD current densities. The ρ meson family mass spectra can be then obtained from Eq. (13) with boundary condition $v_n(0) = 0$, $\lim_{z \rightarrow \infty} v'_n(z) = 0$. The mass spectra is shown in the second and third rows of Table II, respectively for quadratic (Eq. (18)) and deformed (Eq. (19)) dilaton fields [50]. The first column in Table II corresponds to the experimental data in Fig. 1.

ρ vector mesons mass spectra			
n	Exp. (MeV)	mass $_{\Phi_1(z)}$ (MeV)	mass $_{\Phi_2(z)}$ (MeV)
1	775.26 \pm 0.25	727.8	753.9
2	1350 $^{+40}_{-50}$	1134.6	1133.8
3	1465 \pm 25	1426.0	1430.0
4	1570 \pm 98	1534.1	1537.9
5	1720 \pm 20	1664.5	1667.9
6	1909 \pm 30	1873.6	1875.4
7	2149 \pm 17	2061.9	2063.7
8	2265 \pm 40	2233.6	2234.6

TABLE II: The experimental [19] and predicted mass spectra for the ρ vector meson family, in both the quadratic (Eq. (18)) and the deformed (Eq. (19)) dilaton profiles. Respectively along the rows, for the $\rho(770)$, $\rho'(1450)$, $\rho(1450)$, $\rho(1570)$, $\rho(1700)$, $\rho(1900)$, $\rho(2150)$ and $\rho(2270)$ mesons.

Similarly to the ρ mesons, the a_n axial vector mesonic excitations (cf. Eq. (14)) describe the a_1 axial vector meson family, whose mass spectra can be obtained from the modes of the axial gauge field (6b) in the bulk. The quadratic terms in the transverse component of the axial vector \hat{A}^m (6b), denoted by \hat{A}^Γ , are used to construct the

action

$$S_{\hat{A}} = \kappa \int e^{5A - \Phi} \left(\partial_m \hat{A}_\mu^\Gamma \partial^m \hat{A}^{\Gamma\mu} + \frac{4g_5^2 \xi^2}{\ell^2} \hat{A}_\mu^\Gamma \hat{A}^{\Gamma\mu} \right) d^5x, \quad (25)$$

where $g_5^2 = 4\pi^2 N_f/N_c$. The bulk effective mass in (25) is generated by the Higgs mechanism, with the \mathfrak{X} scalar field encoding the chiral symmetry breaking [53]. The EOMs that drive the axial vector mesonic states can be written as Eqs. (14) – (17), with boundary conditions $\lim_{z \rightarrow \infty} a'_n(z) = 0$ and $a_n(0) = 0$. The mass spectra of the a_1 axial vector meson family is shown in the second and third rows of Table III, respectively for quadratic (Eq. (18)) and deformed (Eq. (19)) dilaton fields. The first column in Table III represents the experimental data [19].

a_1 mesons mass spectra			
n	Exp. (MeV)	mass $_{\Phi_1(z)}$ (MeV)	mass $_{\Phi_2(z)}$ (MeV)
1	1255 $^{+13}_{-23}$	1064.9	1117.5
2	1414 $^{+15}_{-13}$	1364.4	1624.1
3	1654 \pm 19	1561.7	1623.0
4	1930 $^{+30}_{-70}$	1845.8	1878.6
5	2096 \pm 138	2059.0	2082.5
6	2265 \pm 50	2242.0	2262.7

TABLE III: The experimental [19] and predicted mass spectra for a_1 axial vector mesons, in both the quadratic (Eq. (18)) and the deformed (Eq. (19)) dilaton profiles. Respectively along the rows, for $a_1(1260)$, $a_1(1420)$, $a_1(1640)$, $a_1(1930)$, $a_1(2095)$ and $a_1(2270)$ mesons.

Now, in order to compute the CE for the f_0 , the ρ , and the a_1 mesons families, and one first considers a localized, Lebesgue-integrable $\epsilon(z)$ energy density, associated to each meson family. In general, given an arbitrary Lagrangian, \mathcal{L} , the energy-momentum tensor reads

$$T^{mn} = \frac{2}{\sqrt{-g}} \left(\frac{\partial(\sqrt{-g}\mathcal{L})}{\partial g_{mn}} - \partial_{x^q} \frac{\partial(\sqrt{-g}\mathcal{L})}{\partial \left(\frac{\partial g_{mn}}{\partial x^q} \right)} \right). \quad (26)$$

The $\epsilon(z)$ energy density corresponds to the $T_{00}(z)$ component of (26), respectively for the f_0 meson family (22), for the ρ meson family (24) and for the a_1 meson family (25). The Fourier transform $\epsilon(k) = \int_{\mathbb{R}} \epsilon(z) e^{-ik \cdot z} dz$, with respect to the z dimension that defines the energy scale in AdS/QCD, is then employed to define the modal fraction [3, 6]

$$\epsilon(k) = \frac{|\epsilon(k)|^2}{\int_{\mathbb{R}} |\epsilon(k)|^2 dk}. \quad (27)$$

It is a correlation probability distribution that quantifies how much a k wave mode contributes to the power spectrum, associated to the energy density. The CE, then,

measures the information content of the spatial profile that characterizes the energy density, $\epsilon(z)$, with respect to the Fourier wave modes. The CE is defined by [3, 6]

$$S[\epsilon] = - \int_{\mathbb{R}} \epsilon_{\diamond}(k) \log \epsilon_{\diamond}(k) dk, \quad (28)$$

for $\epsilon_{\diamond}(k) = \epsilon(k)/\epsilon_{\max}(k)$.

After numerical calculations, the CE is obtained as a function of the n excitation number, $1 \leq n \leq 8$, for the a_1 axial vector, the ρ vector, and the f_0 scalar mesons. The results are listed in Tables IV and V, respectively for the quadratic and deformed dilatonic field backgrounds.

$\Phi_1(z) = \mu_G^2 z^2$			
n	ρ mesons CE	a_1 mesons CE	f_0 mesons CE
1	44.7	468.7	5.64
2	401.8	2.833×10^3	44.28
3	2.408×10^3	1.335×10^4	254.05
4	1.078×10^4	4.859×10^4	1.253×10^3
5	5.336×10^4	2.529×10^5	5.793×10^3
6	2.297×10^5	8.891×10^5	3.196×10^4
7	8.829×10^5	3.462×10^6	1.172×10^5
8	4.589×10^6	1.516×10^7	4.247×10^5

TABLE IV: The CE for the ρ vector, the a_1 axial vector, and the f_0 scalar mesons families, in the $\Phi_1(z) = \mu_G^2 z^2$ quadratic dilaton soft wall model.

$\Phi_2(z) = \mu_G^2 z^2 \tanh(\mu_{G^2}^4 z^2 / \mu_G^2)$			
n	ρ mesons CE	a_1 mesons CE	f_0 mesons CE
1	45.31	669.42	5.84
2	412.83	2.935×10^3	48.21
3	2.821×10^3	1.711×10^4	301.55
4	1.383×10^4	8.013×10^4	1.752×10^3
5	6.366×10^4	3.414×10^5	9.821×10^3
6	2.697×10^5	1.948×10^6	6.277×10^4
7	1.298×10^6	7.962×10^6	2.973×10^5
8	5.822×10^6	3.927×10^7	2.024×10^6

TABLE V: The CE for the ρ vector, the a_1 axial vector, and the f_0 scalar mesons families, in the $\Phi_2(z) = z^2 \tanh\left(\frac{\mu_{G^2}^4 z^2}{\mu_G^2}\right)$ deformed dilaton soft wall model.

In both Tables IV and V, respectively along the rows, the first column is depicted for the ρ vector meson family, identifying the v_n eigenfunctions in Eq. (13) as $v_1 = \rho(770)$, $v_2 = \rho'(1450)$, $v_3 = \rho(1450)$, $v_4 = \rho(1570)$, $v_5 = \rho(1700)$, $v_6 = \rho(1900)$, $v_7 = \rho(2150)$ and $v_8 = \rho(2270)$. The second columns in Tables IV and V are composed by

the a_n eigenfunctions in Eq. (14), describing the a_1 axial vector meson family by the identification $a_1 = a_1(1260)$, $a_2 = a_1(1420)$, $a_3 = a_1(1640)$, $a_4 = a_1(1930)$, $a_5 = a_1(2095)$ and $a_6 = a_1(2270)$. The mesonic excitations a_7 and a_8 are solutions of the EOM (12), for $n = 7$ and $n = 8$, not detected yet. Besides, the third columns in Tables IV and V show the f_0 scalar meson family, described by the s_n wave eigenfunctions of Eq. (12). They read $s_1 = f_0(500)$, $s_2 = f_0(980)$, $s_3 = f_0(1370)$, $s_4 = f_0(1500)$, $s_5 = f_0(1710)$, $s_6 = f_0(2020)$, $s_7 = f_0(2200)$ and $s_8 = f_0(2330)$.

Firstly analyzing the quadratic dilatonic potential in Eq. (18), let one takes the CE for the ρ , a_1 , and f_0 meson families listed in Table IV. Computing the logarithm of the CE for each n mode for the three mesons families leads to the result depicted in Fig. 4, whose numerical interpolation provides the first type of informational entropic Regge trajectories. For the ρ vector, the a_1 axial vector, and the f_0 scalar meson families, respectively, the informational entropic Regge trajectories are the dotted lines in Fig. 4.

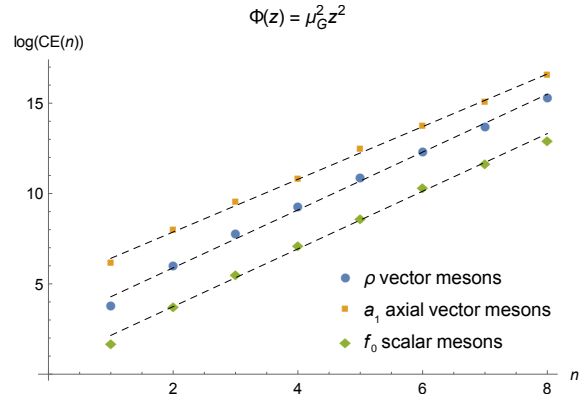


FIG. 4: Logarithm of the configurational entropy of mesons, the families of ρ , a_1 , and f_0 mesons, in the quadratic dilaton soft wall model.

Their explicit expressions are, respectively,

$$\log(\text{CE}_\rho(n)) = 1.6015 n + 2.6844, \quad (29)$$

$$\log(\text{CE}_{a_1}(n)) = 1.4580 n + 4.9540, \quad (30)$$

$$\log(\text{CE}_{f_0}(n)) = 1.5957 n + 0.5517, \quad (31)$$

within respectively 1%, 1.3%, and $\sim 1.9\%$ standard deviations.

Now, with the computed CE for the ρ , a_1 , and f_0 meson families in the Φ_2 dilaton background (19), listed in Table V, one can also calculate the logarithm of the CE, for each n excitation mode. Fig. 5 shows the corresponding results for each meson family, wherein linear regression yields the second type of informational entropic Regge trajectories.

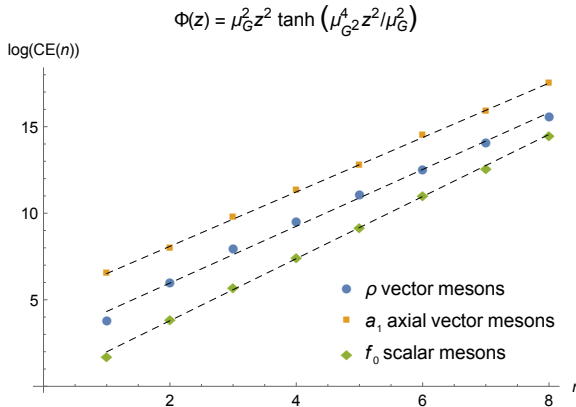


FIG. 5: Logarithm of the configurational entropy of the families of ρ , a_1 , and f_0 mesons, in the deformed soft wall AdS/QCD.

The explicit expressions for each informational entropic Regge trajectory is numerically obtained by interpolation of the data in Table V. The obtained linear regressions, respectively for the a_1 axial vector, the ρ vector, and the f_0 scalar mesons families, read

$$\log(\text{CE}_\rho(n)) = 1.6407 n + 2.6840, \quad (32)$$

$$\log(\text{CE}_{a_1}(n)) = 1.5719 n + 4.9540, \quad (33)$$

$$\log(\text{CE}_{f_0}(n)) = 1.7936 n + 0.2014, \quad (34)$$

within $\sim 0.6\%$, $\sim 1.5\%$, and $\sim 1.9\%$ standard deviations, respectively.

For the ρ , a_1 , and f_0 mesons families, one can hence realize a scaling law, relating the logarithm of the CE and the n meson excitation modes. Figs. 4 and 5 show that there are informational entropic Regge trajectories, implementing a relation between the logarithm of the CE and the n excitation number, for both the quadratic and deformed dilatonic potentials.

The original Regge trajectories in the soft wall AdS/QCD regard the relation $m_n \sim n$, for the light-flavor meson mass spectra. One can then emulate them in the information entropic context. In fact, one can calculate the logarithm of the CE for each meson family, as a function of the meson mass spectra, experimentally detected. In what follows, the $\Phi_2(z) = z^2 \tanh\left(\frac{\mu_G^4 z^2}{\mu_G^2}\right)$ deformed dilaton in the soft wall AdS/QCD model shall be employed, as it better describes the meson mass spectra. The results are plotted in Fig. 6.

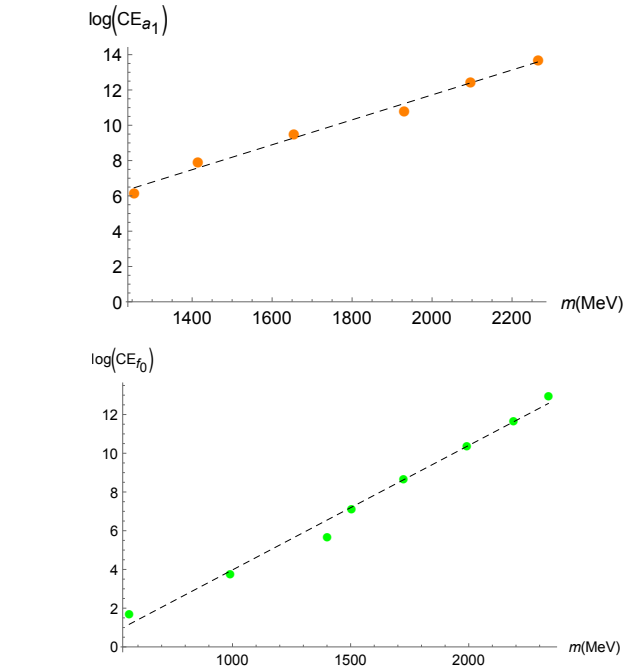
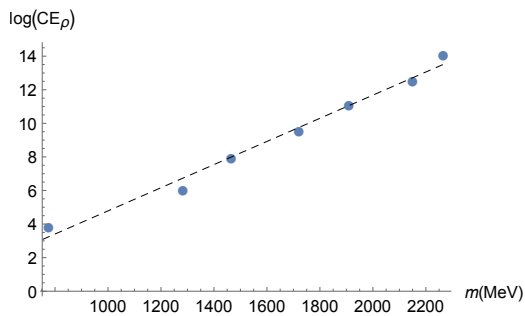


FIG. 6: Logarithm of the configurational entropy of the ρ (blue), a_1 , (orange), and f_0 (green) mesons families, as a function of their mass spectra. The respective informational entropic Regge trajectories are also plotted.

The informational entropic Regge trajectories, as a function of the meson mass, m (MeV), are respectively listed as follows:

$$\log(\text{CE}_\rho(m)) = 0.0069 m - 2.109, \quad (35)$$

$$\log(\text{CE}_{a_1}(m)) = 0.0071 m - 2.403, \quad (36)$$

$$\log(\text{CE}_{f_0}(m)) = 0.0064 m - 2.452, \quad (37)$$

within $\sim 3\%$, $\sim 2.3\%$, and $\sim 3.5\%$ standard deviations, respectively. The informational entropic Regge trajectories in Eqs. (35) – (37) bring another very interesting aspect of the CE that underlies the meson families. Instead of computing the meson family mass spectra, solving Eqs. (12) – (14), one can extrapolate the interpolation lines (32) – (34) to compute the CE for the meson families, at least for the n mesonic excitations such that $n > 8$, for the ρ and f_0 families, and such that $n > 6$, for the a_1 family.

In the following discussion of the informational entropic Regge trajectories (32) – (34), the notation $m_{\alpha,n}$ means the mass of the n^{th} meson in some α -meson family ($\alpha = \rho, a_1, f_0$), corresponding to the element in the respective meson family with n excitation number. Considering the experimental of the ρ vector meson family, although there is no mesonic excitation v_n in the ρ meson family higher than $n = 8$, experimentally detected, the informational entropic Regge trajectory in Fig. 6 deploys a reliable method for predicting the mass of the v_n vector meson states, for $n \geq 9$. Although the explicit calculation by Eq. (13), with potential (16), is

already known to produce the mass spectra of the ρ vector meson family, as a function of the n excitation number, here the masses of the v_9 and v_{10} elements in the ρ meson mass family can be then inferred. In fact, for $n = 9$, Eq. (32) yields $\log(\text{CE}_\rho) = 17.450$. Replacing this value in the informational entropic Regge trajectory (35), one obtains the mass $m_{\rho,9} = 2834.68$ MeV, for the v_9 mesonic state in the ρ meson family. The standard deviations for Eqs. (32) – (35) gives the reliable range $2767 \text{ MeV} \lesssim m_{\rho,9} \lesssim 2901$ MeV, for the v_9 vector meson state. Similarly, the v_{10} vector meson excitation has mass $m_{\rho,10} = 3072$ MeV. Considering the standard deviations for Eqs. (32) – (35), the range $3009 \lesssim m_{\rho,10} \lesssim 3135$ MeV is a reliable one. One can further extrapolate the mass spectra for the v_n vector mesonic excitations, for $n \geq 11$, however the standard deviations are larger, the higher the n excitation number is.

Analogously, the a_1 axial vector meson family can be analyzed. The masses of the a_7 and a_8 can be then inferred, using the mass spectra of the experimentally detected mesons in this family, using Eq. (33) – (36). In fact, for $n = 7$, Eq. (33) yields $\log(\text{CE}_{a_1}) = 15.957$. Replacing this value in the informational entropic Regge trajectory (35), one obtains the mass $m_{a_1,7} = 2586$ MeV, for the a_7 mesonic state in the a_1 meson family. The standard deviations for Eqs. (33) and (36) gives the reliable range $2510 \text{ MeV} \lesssim m_{a_1,7} \lesssim 2660$ MeV, for the a_7 axial vector meson state. Similarly, the a_8 vector meson excitation has mass $m_{a_1,8} = 2807$ MeV. The standard deviations for Eqs. (32) and (35) yield the range $2726 \lesssim m_{a_1,8} \lesssim 2888$ MeV. One can further infer the mass spectra of the a_n vector mesonic excitations, for $n \geq 9$.

Finally, the masses of the next generation of f_0 scalar mesons, can be predicted. Employing Eq. (34), for $n = 9$ implies that $\log(\text{CE}_{f_0}) = 16.344$. Now, one can substitute this value into Eq. (37), yielding the mass of the s_9 element in the f_0 meson family, $m_{f_0,9} = 2936$ MeV. The standard deviations for Eqs. (34) – (37) gives the reliable range $2841 \text{ MeV} \lesssim m_{f_0,9} \lesssim 3030$ MeV, for the s_9 scalar mesonic excitation. Besides, similar calculations yield the s_{10} scalar meson excitation mass, $m_{f_0,10} = 3217$ MeV. The standard deviations related to Eqs. (32) and (35) imply the range $3105 \lesssim m_{f_0,10} \lesssim 3329$ MeV, for the s_{10} scalar meson. One can further extrapolate the mass spectra of the s_n scalar mesonic excitations, for $n \geq 11$, however the standard deviations increase, the higher the n excitation number is.

V. CONCLUDING REMARKS AND PERSPECTIVES

The CE was computed for a_1 axial vector, the ρ vector, and the f_0 scalar mesons families, for two dilatonic backgrounds, in a graviton-dilaton-gluon background. Two types of informational entropic Regge trajectories were derived, for each meson family. The first one consists

of the CE in terms of the meson n excitation number, described by Eqs. (32) – (34) and illustrated in Figs. 4 and 5, for both quadratic and deformed dilatonic profiles. The second type of informational entropic Regge trajectories relates the logarithm of the CE to the experimental mass spectra of the mesons families, in Eqs. (35) – (37), respectively shown in the plots of Fig. 6. Consequently, the mesons families mass spectra were extrapolated from these informational entropic Regge trajectories. A range for the mass spectra of mesons with higher n excitation numbers, in each meson family, was then estimated with good accuracy. The two first elements of the next generation, in each meson family, were studied and discussed.

The prediction of the meson mass spectra through Eqs. (12) – (14), although also taking experimental parameters to fit the meson mass spectra, is a theoretical prediction, that already matches experimental data, as shown in Ref. [50] and illustrated in Tables I – III. On the hand, the very essence of procedure throughout Sect. IV estimates the mass spectra of the next generation of mesons by the informational entropic Regge trajectories, based on the mass spectra of the already detected mesons. Indeed, the first types (32) – (34) of informational entropic Regge trajectories express the CE, once the n excitation number is fixed. With the obtained value of the CE, Eqs. (35) – (37) then determine the values of the masses of the next generation of mesonic states, in each ρ , a_1 , and f_0 family. Since the informational entropic Regge trajectories are determined by the experimental meson mass spectra, then this procedure can determine at least the two next elements in each meson family, with good accuracy. The eventual detection of these new mesonic states shall contribute with more experimental points in the plots of Fig. 6, improving the fitting of Eqs. (35) – (37).

Pseudo-scalar mesons can be further regarded, whose CE may be also computed. However, their Lagrangian involves a pseudo-scalar field that is coupled to a φ scalar field that defines the parallel axial vector (complementary to the transverse to the \dot{A}_μ^Γ field in (22)) as $\partial_\mu\varphi$. Hence, the derived coupled system of EOMs involve awkward Schrödinger-like potentials, turning the CE computation a hard task, unsolved up to now. Besides, as the soft wall AdS/QCD model corresponds to the D_3 - D_q , system, extensions involving D_p - D_q models [54] may be also accomplishable, although it is far beyond the scope here assumed. Finite temperature effects in the soft wall AdS/QCD may be also implemented, as whose initial results using the CE apparatus were introduced in Ref. [55] for quarkonia.

Acknowledgments: The work of AEB is supported by the Brazilian Agencies FAPESP (grant 2018/03960-9) and CNPq (grant 300831/2016-1). RdR is grateful to FAPESP (Grant No. 2017/18897-8) and to the National Council for Scientific and Technological Development – CNPq (Grant No. 303293/2015-2), for partial financial support.

[1] C. E. Shannon, Bell Syst. Tech. J. **27** (1948) 379; 623.

[2] M. Gleiser and N. Stamatopoulos, Phys. Lett. B **713** (2012) 304 [arXiv:1111.5597 [hep-th]].

[3] M. Gleiser and N. Stamatopoulos, Phys. Rev. D **86** (2012) 045004 [arXiv:1205.3061 [hep-th]].

[4] M. Gleiser, M. Stephens and D. Sowinski, Phys. Rev. D **97** (2018) 096007 [arXiv:1803.08550 [hep-th]].

[5] M. Gleiser and N. Graham, Phys. Rev. D **89** (2014) 083502 [arXiv:1401.6225 [astro-ph.CO]].

[6] M. Gleiser and D. Sowinski, Phys. Lett. B **747** (2015) 125 [arXiv:1501.06800 [cond-mat.stat-mech]].

[7] A. E. Bernardini and R. da Rocha, Phys. Lett. B **762** (2016) 107 [arXiv:1605.00294 [hep-th]].

[8] A. E. Bernardini, N. R. F. Braga and R. da Rocha, Phys. Lett. B **765** (2017) 81 [arXiv:1609.01258v1 [hep-th]].

[9] N. R. F. Braga and R. da Rocha, Phys. Lett. B **776** (2018) 78 [arXiv:1710.07383 [hep-th]].

[10] D. Sowinski and M. Gleiser, J. Stat. Phys. **167** (2017) no.5, 1221 [arXiv:1606.09641 [cond-mat.stat-mech]].

[11] N. R. F. Braga and R. da Rocha, Phys. Lett. B **767** (2017) 386 [arXiv:1612.03289 [hep-th]].

[12] E. Witten, *A Mini-Introduction To Information Theory*, [arXiv:1805.11965 [hep-th]].

[13] M. Natsume, “AdS/CFT Duality User Guide,” Lect. Notes Phys. **903** (2015) 1 [arXiv:1409.3575 [hep-th]].

[14] J. Polchinski and M. J. Strassler, Phys. Rev. Lett. **88** (2002) 031601 [arXiv:hep-th/0109174].

[15] H. Boschi-Filho and N. R. F. Braga, Eur. Phys. J. C **32** (2004) 529 [arXiv:hep-th/0209080].

[16] C. Csaki and M. Reece, JHEP **05** (2007) 062 [arXiv:hep-ph/0608266].

[17] A. Karch, E. Katz, D. T. Son and M. A. Stephanov, Phys. Rev. D **74** (2006) 015005 [hep-ph/0602229].

[18] S. J. Brodsky, G. F. de Teramond, H. G. Dosch, J. Erlich, Phys. Rept. **584** (2015) 1 [arXiv:1407.8131 [hep-ph]].

[19] M. Tanabashi *et al.* [ParticleDataGroup], Phys. Rev. D **98** (2018) 030001.

[20] T. Gherghetta, J. I. Kapusta and T. M. Kelley, Phys. Rev. D **79** (2009) 076003 [arXiv:0902.1998 [hep-ph]].

[21] L. Da Rold and A. Pomarol, Nucl. Phys. B **721** (2005) 79 [arXiv:hep-ph/0501218].

[22] P. Zhang, JHEP **1005** (2010) 039 [arXiv:1003.0558].

[23] Y. -Q. Sui, Y. -L. Wu, Z. -F. Xie and Y. -B. Yang, Phys. Rev. D **81** (2010) 014024 [arXiv:0909.3887 [hep-ph]].

[24] G. 't Hooft, Nucl. Phys. B **72** (1974) 461.

[25] N. Barbosa-Cendejas, R. Cartas-Fuentevilla, A. Herrera-Aguilar, R. R. Mora-Luna and R. da Rocha, Phys. Lett. B **782** (2018) 607 [arXiv:1805.04485 [hep-th]].

[26] N. R. F. Braga, L. F. Ferreira and R. da Rocha, *Thermal dissociation of heavy mesons and configurational entropy*, [arXiv:1808.10499 [hep-ph]].

[27] A. Goncalves and R. da Rocha, Phys. Lett. B **774** (2017) 98 [arXiv:1706.01482 [hep-ph]].

[28] G. Karapetyan, Phys. Lett. B **781** (2018) 201 [arXiv:1802.09105 [nucl-th]].

[29] G. Karapetyan, Phys. Lett. B **787** (2018), to appear [arXiv:1807.04540 [nucl-th]].

[30] G. Karapetyan, EPL **117** (2017) 18001 [arXiv:1612.09564 [hep-ph]].

[31] G. Karapetyan, EPL **118** (2017) 38001 [arXiv:1705.10617 [hep-ph]].

[32] C. W. Ma, Y. G. Ma, Prog. Part. Nucl. Phys. **99** (2018) 120 [arXiv:1801.02192 [nucl-th]].

[33] M. Gleiser and D. Sowinski, Phys. Lett. B **727** (2013) 272 [arXiv:1307.0530 [hep-th]].

[34] M. Gleiser and N. Jiang, Phys. Rev. D **92** (2015) 044046 [arXiv:1506.05722 [gr-qc]].

[35] R. Casadio and R. da Rocha, Phys. Lett. B **763** (2016) 434 [arXiv:1610.01572 [hep-th]].

[36] R. A. C. Correa and R. da Rocha, Eur. Phys. J. C **75** (2015) 522.

[37] R. A. C. Correa, D. M. Dantas, C. A. S. Almeida and R. da Rocha, Phys. Lett. B **755** (2016) 358 [arXiv:1601.00076 [hep-th]].

[38] A. Alves, A. G. Dias, R. da Silva, Braz. J. Phys. **47** (2017) 426 [arXiv:1703.02061 [hep-ph]].

[39] A. Alves, A. G. Dias, R. da Silva, Physica **420** (2015) 1 [arXiv:1408.0827 [hep-ph]].

[40] N. R. F. Braga, M. A. M. Contreras and S. Diles, Phys. Lett. B **763** (2016) 203 [arXiv:1507.04708 [hep-th]].

[41] P. Colangelo, F. De Fazio, F. Giannuzzi, F. Jugeau and S. Nicotri, Phys. Rev. D **78** (2008) 055009 [arXiv:0807.1054 [hep-ph]].

[42] S. S. Afonin, Phys. Lett. B **719** (2013) 399 [arXiv:1210.5210 [hep-ph]].

[43] R. Rougemont, R. Critelli, J. Noronha-Hostler, J. Noronha and C. Ratti, Phys. Rev. D **96** (2017) 014032 [arXiv:1704.05558 [hep-ph]].

[44] W. de Paula, T. Frederico, H. Forkel and M. Beyer, Phys. Rev. D **79** (2009) 075019 [arXiv:0806.3830 [hep-ph]].

[45] W. de Paula and T. Frederico, Phys. Lett. B **693** (2010) 287 [arXiv:0908.4282 [hep-ph]].

[46] E. Folco Capossoli, D. Li and H. Boschi-Filho, Eur. Phys. J. C **76** (2016) 320 [arXiv:1604.01647 [hep-ph]].

[47] M. Ihl, M. Torres, H. Boschi-Filho and C. A. B. Bayona, JHEP **1109** (2011) 026 [arXiv:1010.0993 [hep-th]].

[48] B. Batell, T. Gherghetta and D. Sword, Phys. Rev. D **78** (2008) 116011 [arXiv:0808.3977 [hep-ph]].

[49] C. A. Ballon Bayona, H. Boschi-Filho and N. R. F. Braga, JHEP **0803** (2008) 064 [arXiv:0711.0221 [hep-th]].

[50] D. Li and M. Huang, JHEP **1311** (2013) 088 [arXiv:1303.6929 [hep-ph]].

[51] F. Xu and M. Huang, Chin. Phys. C **37** (2013) 014103 [arXiv:1111.5152 [hep-ph]].

[52] A. Cherman, T. D. Cohen and E. S. Werbos, Phys. Rev. C **79** (2009) 045203 [arXiv:0804.1096 [hep-ph]].

[53] J. Erlich, E. Katz, D. T. Son and M. A. Stephanov, Phys. Rev. Lett. **95** (2005) 261602 [arXiv:hep-ph/0501128].

[54] S. He, M. Huang, Q. S. Yan and Y. Yang, Eur. Phys. J. C **66** (2010) 187 [arXiv:0710.0988 [hep-ph]].

[55] N. R. F. Braga and L. F. Ferreira, Phys. Rev. D **94** (2016) 094019 [arXiv:1606.09535 [hep-th]].